

# High Spatial Resolution in Vertical Slice Ocean Acoustic Tomography

BRUCE CORNUELLE AND BRUCE M. HOWE

*Scripps Institution of Oceanography, University of California, San Diego, La Jolla*

Most studies of ocean acoustic tomography have assumed that little horizontal information is available from the many acoustic multipath travel times observed in a single vertical plane (slice) between source and receiver moorings. There is in fact significant small-scale information present in such data sets. We examine single vertical slice tomography in spectral terms, and show that the acoustic measurements resemble a high-pass filter, which is more sensitive to small scales (shorter than 100 km) than to longer scales, with the exception of the mean, which is well measured. The sensitivity extends to scales smaller than 10 km, in theory, although the level of the ocean energy spectrum is so low at these scales that even small data errors limit the measurement. We use analytical calculations supplemented by numerical simulations with realistic data sets to show that accurate reconstructions of the high wave number features are possible out to the limits of the parameterization (9.2-km wavelength) when the power spectrum of the ocean features is white or red, the total measurement error is 1 ms, and multiple receivers are used. The ultimate limit of spatial resolution may be smaller still, depending on array configuration, measurement errors, and the shape of the power spectrum.

## INTRODUCTION

Away from the source and receiver, an acoustic ray path in the ocean (multipath) is periodic over a distance called the "double-loop range." The sensitivity of the acoustic travel time along a ray path to an ocean feature depends on the projection of the ocean feature on the path. Features which match the ray periodicity have strong effects on travel time compared to other components, so sampling by a set of multipaths with different double-loop ranges can be understood in terms of Fourier integrals. The typical ocean sound speed profile allows a maximum double-loop range of less than 100 km, so if the reconstruction of a single section is considered in spectral terms, there is a gap in the information available from the multipaths in a typical vertical slice. While the spatial mean between source and receiver is well measured, features with scales less than the transmission range but greater than the ray double-loop range are poorly sampled. At scales comparable to the maximum ray double-loop range (usually about 80 km), the sensitivity improves, and useful information is available down to scales smaller than 10 km.

This high-pass information could have a variety of applications, including feature identification, repeated high wave number spectra over large areas, and fine-scale dynamical studies. The availability of this information may suggest changes in present tomographic data processing and array design.

This discussion will have four main parts: (1) a summary of the ocean acoustic tomography problem; (2) analytical theory describing the sensitivity of ocean tomography data to spectral functions in a single section between source and receiver moorings; (3) numerical calculations of sensitivity using a realistic ocean section to check the predictions; and (4) inverse estimates of horizontal structure using simulated multipath data.

Copyright 1987 by the American Geophysical Union.

Paper number 7C0588.  
0148-0227/87/007C-0588\$05.00

## OCEAN ACOUSTICS

A typical sound speed profile for the North Atlantic southwest of Bermuda has a sound speed minimum at a depth of about 1 km (Figure 1). This minimum acts as a geometrically dispersive waveguide ("sound channel") which allows distinct acoustic ray paths between a single source and receiver. Figure 2 shows a set of 24 multipaths for a single source and receiver separated by 600 km computed using a ray-tracing program for the sound speed profile of Figure 1. Sound energy transmitted from source to receiver along different multipaths will in general require different travel times to complete the journey. If sufficiently narrow pulses are transmitted, the different ray paths can be distinguished by their arrival times. Figure 3 shows a set of pulse arrivals for the rays shown in Figure 2 as calculated by the WKBJ method of *Brown* [1982].

The ray paths oscillate around the sound speed minimum ("channel axis") with turning points above and below the axis. The double-loop range is the length in which the ray path makes one complete cycle above and below the axis (two turning points). It ranges from a minimum of about 20 km for rays which remain near the axis to a maximum of about 80 km for rays which nearly hit the surface and/or bottom.

A pulse traveling from a source to a receiver through an ocean with sound speed  $c(x, y, z)$  will follow one of a number of possible ray paths,  $\zeta_k$ , determined by that sound speed field. The measured source to receiver travel time  $T_k$  (for path  $\zeta_k$ ) is given by

$$T_k(t) = \int_{\zeta_k} \frac{ds}{c(x, y, z, t)} + E_k \quad (1)$$

where  $s$  is the arc length along the ray path, and  $E_k$  is an error term which includes travel time errors due to clock drift, travel time errors due to source-receiver position uncertainty, which arise from uncorrected mooring motion, errors due to unmodeled ocean features (such as fine scale internal waves), and uncertainties in arrival time determination. The tomographic data are the travel times

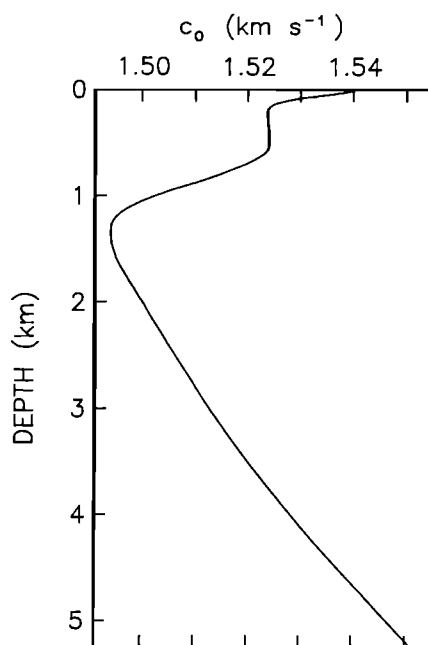


Fig. 1. Sound speed profile for the North Atlantic southwest of Bermuda. This profile was used for all the ray calculations in the study.

$T_k$  for sound pulses traveling along the various distinct paths.

For small sound speed perturbations, the expression for travel time (equation (1)) can be linearized around a basic state,  $c_0(x, y, z)$ . Let

$$c(x, y, z) \equiv c_0(x, y, z) + c'(x, y, z) \quad (2)$$

where  $c'$ , the sound speed perturbation, is small compared to  $c_0$ . To first order, the expression for travel time perturbation becomes

$$T'_k = T_k - T_k^0 = - \int_{\zeta_k^0} \frac{c'(x, y, z) ds}{c_0^2(x, y, z)} + E_k \quad (3)$$

where  $\zeta_k^0$  is the ray path for the basic state  $c_0$ ,  $T_k^0$  is the travel time for the ray in the basic state, and  $T'_k$  is the perturbation in observed travel time. Equation (3) is linear,

so linear inverse techniques can be used to infer  $c'$ , given a data set  $\{T'_k\}$ .

All the tomography experiments to date have used linear inverse methods based on least squares optimization [Ocean Tomography Group, 1982; Cornuelle et al., 1985; Howe et al., 1987]. These methods are generalizations of optimal interpolation which require prior estimates of the statistics of the data error and of the statistics of the model parameters. For simultaneous data, the inversion yields an estimate of the unknown fields and an estimate of the covariance of the errors in the estimates. The latter is used here to quantify the resolving power of the data. However, even before invoking the inverse, rough resolution estimates can be made by examining the availability of data sensitive to a given spectral component of ocean variation.

If the travel time data are sensitive to a particular model function, the corresponding ocean structure is likely to be well resolved. Conversely, if the travel time data are not sensitive to a particular model function, the inverse reconstruction ignores that structure unless a covariance between model functions is imposed. No prior covariances between model parameters were specified here, so lack of sensitivity to a particular model parameter means that that parameter will be poorly reconstructed.

In the equations above, the effect of ocean currents has been neglected. The component of current tangent to the ray path affects travel time like a sound speed perturbation, but current velocities are generally less than  $50 \text{ cm s}^{-1}$ , small in comparison to the expected sound speed perturbations of the order of  $5 \text{ m s}^{-1}$ . In practice, the velocity contributions are included in the forward problem, but are not well estimated by the inverse procedure because they are so much less than the dominant sound speed contribution. However, if two oppositely directed ray paths are available between transceivers, then the difference of their travel time perturbations is only sensitive to the tangent component of the current integrated along the ray path, because the sound speed contributions are the same in each direction and cancel. The estimation can proceed separately for sum and difference travel times, eliminating the cross-talk between sound speed and current which otherwise degrades the estimates of current. This technique is called reciprocal

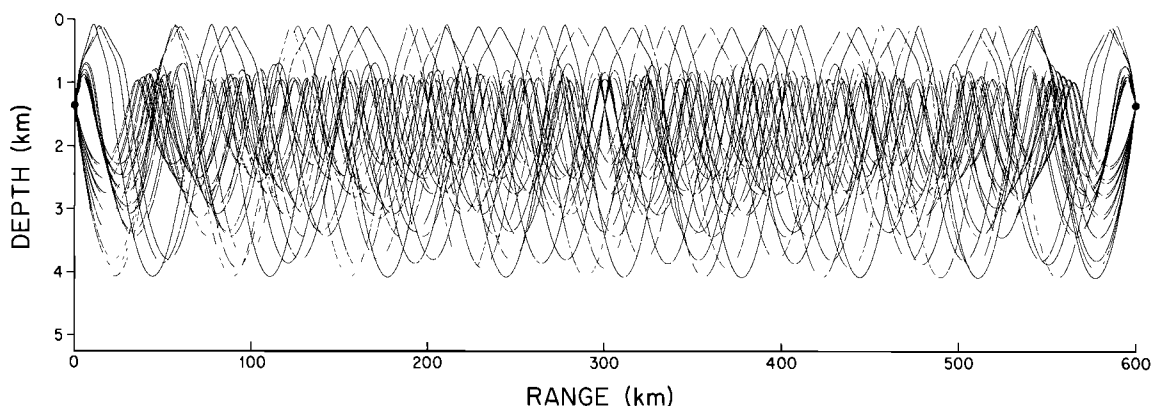


Fig. 2. Twenty-four multipaths for a single source and receiver (both at 1350 m) traced in the sound speed profile of Figure 1. The range is 600 km and the ocean depth is 5.25 km.

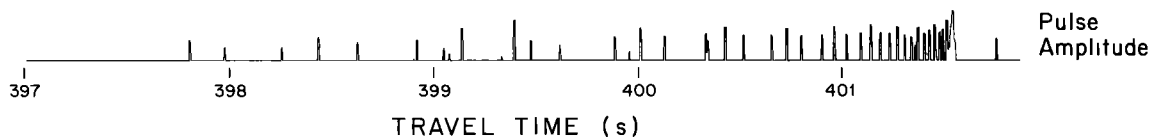


Fig. 3. The pattern of pulse arrivals (pressure amplitude) for the rays shown in Figure 2. The amplitude of the pulses is for relative comparison only.

tomography (or "velocity" tomography) as opposed to one-way or "density" tomography, and has been the focus of the most recent experiments [Howe *et al.*, 1987]. The analysis below applies to reciprocal tomography if the difference between reciprocal travel time perturbations is substituted for the one-way perturbation, and the parameterization then represents velocity in the plane of the measurements, with positive velocity directed toward the receiver. Because of the low aspect ratio (shallow angle) of the rays, the effect of the dot product in the tangent projection can be neglected. In practice, since the velocity signals are weaker than the sound speed signals, the inverse for velocity is more sensitive to data error.

#### ANALYTICAL DISCUSSION OF RESOLUTION

For simplicity, we will restrict the problem to observing the ocean between a single pair of moorings, so the only horizontal coordinate is  $r$ , the horizontal range from the source, and we will assume that the reference state is horizontally uniform,  $c_0(r, z) = c_0(z)$ . We parameterize ("model")  $c'(r, z)$  using two sets of spectral functions: sinusoids in the horizontal and a limited set of special functions  $F_i(z)$  in the vertical. These vertical structure functions (or "modes") can be (1) calculated analytically as solutions of the quasi-geostrophic vertical structure equation, (2) obtained statistically by computing empirical orthogonal functions (EOFs) from a data set, or (3) they may be picked arbitrarily, as in a set of functions defining layers with unit amplitude within the layer and zero outside. The dynamical modes and the EOFs have the advantage that relatively few are needed to describe the vertical structure in a limited region. Many more of the arbitrary functions must generally be used to reproduce the ocean accurately, but the parameterization is independent of location. We generally lack good estimates of the vertical covariance functions, but because here we are considering specific areas of ocean, we can select dynamically calculated modes which will limit the number of model parameters. Figure 4 shows the set of dynamical modes for sound speed and velocity used in the parameterization. These modes were calculated using the same oceanographic data used to calculate the sound speed profile in Figure 1. They were calculated in the low-frequency limit, so the vertical structure is independent of horizontal wave number. The dependence on horizontal wave number might be retained to include internal waves.

Combining the vertical and horizontal expansions, the sound speed (or current) perturbation at any point,  $(r, z)$  is

$$c'(r, z) = \sum_{i=1}^N \sum_{j=1}^M [a_{ij} \cos(\frac{2\pi jr}{R}) + b_{ij} \sin(\frac{2\pi jr}{R})] F_i(z) \quad (4)$$

where  $R$  is the range to the receiver. The sinusoids can

be chosen to have any fundamental period; the use of  $R$  merely simplifies some of the algebra to come. Rewriting equation (3) by denoting the ray depth as a function of range by  $\zeta_k(r)$  and by changing variables in the integration from arc length to range gives

$$T'_k = - \int_0^R \frac{c'[r, \zeta_k(r)] [1 + (\frac{d\zeta_k}{dr})^2]^{1/2} dr}{c_0^2[\zeta_k(r)]} + E_k \quad (5)$$

Substituting (4) into (5) then gives

$$T'_k = - \int_0^R \sum_{i=1}^N \sum_{j=1}^M [a_{ij} \cos(\frac{2\pi jr}{R}) + b_{ij} \sin(\frac{2\pi jr}{R})] \frac{F_i[\zeta_k(r)] [1 + (\frac{d\zeta_k}{dr})^2]^{1/2} dr}{c_0^2[\zeta_k(r)]} + E_k \quad (6)$$

Equation (6) shows that the information available in the tomographic data depends on the harmonic structure of the function  $G_{ik}(r)$ :

$$G_{ik}(r) = \frac{F_i[\zeta_k(r)] [1 + (\frac{d\zeta_k}{dr})^2]^{1/2}}{c_0^2[\zeta_k(r)]} \quad (7)$$

This quantity, the projection of the ray on a given vertical mode, will be called the "ray weighting function." A similar concept describing ray travel time variances was introduced to calculate the sensitivity of travel time variance to internal wave spectra [Flatté and Stoughton, 1986]. The weighting function describes where in physical space the amplitude of mode  $i$  affects the travel time for ray  $k$ , whether or not a spectral expansion is used for the model. To derive the sensitivity of the data to the spectral functions of the model, we perform sine and cosine transforms

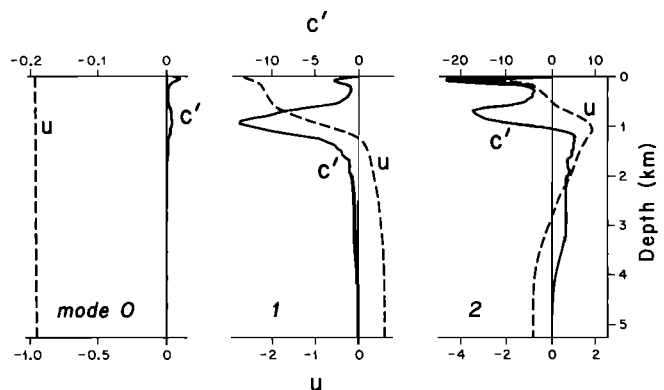


Fig. 4. Dynamical modes for sound speed (solid line) and current (dashed line) calculated using the same data as for Figure 1. The mode labeled "0" is the barotropic mode, which has an insignificant sound speed contribution. Mode 1 is the first baroclinic mode, and mode 2 is the second baroclinic mode.

of  $G_{ik}(r)$ :

$$T'_k = - \sum_{i=1}^N \sum_{j=1}^M \left[ a_{ij} \int_0^R \cos\left(\frac{2\pi jr}{R}\right) G_{ik}(r) dr + b_{ij} \int_0^R \sin\left(\frac{2\pi jr}{R}\right) G_{ik}(r) dr \right] + E_k \quad (8)$$

The variation of the denominator in (7) is small ( $< 6\%$ ) over the ray path, and may be neglected. The arc length correction term  $d\zeta_k/dr$  ( $< 3\%$ ) is also ignored in this discussion, so  $G_{ik}(r)$  is equal to  $F_i[\zeta_k(r)]$ . The fundamental periodicity of this function is controlled by the ray loop length, and the combination of nonlinear vertical mode profile  $F_i(z)$  and nonsinusoidal ray path  $\zeta_k$  contribute to a rich spectrum of harmonics.

Assume for simplicity that the source and receiver are both on the sound channel axis and that the path of ray  $k$  is a sinusoid in range around the sound channel axis,  $z = z_0$ , with depth as a function of range given by

$$\zeta_k(r) = \beta_k \sin\left(\frac{\pi kr}{R}\right) + z_0 \quad (9)$$

where  $k$  is the number of turning points for the ray, and  $\beta_k$  is the amplitude of the ray excursions around the sound channel axis. There are two possible rays with  $k$  turning points, one with positive launch angle (above the axis), and the other with negative launch angle, but the second ray is redundant in this idealized case because the paths are exactly symmetric around the sound speed minimum. (In general, the sound speed minimum is not symmetric, and neither are the rays, so downward going rays contribute useful information.) Expanding  $F_i$  as a polynomial in  $(z - z_0)$ ,

$$F_i(z) = \sum_{n=0}^{\infty} \alpha_n (z - z_0)^n \quad (10)$$

one can substitute into (7), and look (for the term with exponent  $n$ ) at the dependence of travel time on the cosine and sine amplitudes, respectively, of the model function with wave number  $j$ :

$$\left(\frac{\partial T'_k}{\partial a_{ij}}\right)_n = -\alpha_n \beta_k^n \int_0^R \cos\left(\frac{2\pi jr}{R}\right) [\sin\left(\frac{\pi kr}{R}\right)]^n dr \quad (11)$$

and

$$\left(\frac{\partial T'_k}{\partial b_{ij}}\right)_n = -\alpha_n \beta_k^n \int_0^R \sin\left(\frac{2\pi jr}{R}\right) [\sin\left(\frac{\pi kr}{R}\right)]^n dr \quad (12)$$

Equations (11) and (12) contain much information about the problem of observing and reconstructing ocean features using acoustic multipath travel times. For depth-independent structure ( $n = 0$ ), only the cosine term with  $j = 0$  (the range average) affects the travel time. If mode  $i$  for sound speed (or current, if these are reciprocal rays) is entirely depth independent, then the data are insensitive to all range-dependent structures of the mode, regardless of ray shape. (For precise calculations, the arc length and sound speed dependence in (7) must be included, so some horizontal information is available even for a barotropic mode.) Axial rays generally have the largest numbers of turning points ( $k$ ), so the dependence on  $\beta_k$  suggests a decline in sensitivity as  $k$  increases for a given source-

receiver pair. For  $n = 1$  and  $k$  even, the travel time contribution is zero for all model parameters except  $b_{ij}$  with  $j = k/2$ , so the cosine term in the model will be completely ignored. The cosine term can be picked up by adding a source and receiver at  $\beta_k$  above or below the axis. For  $n = 1$  and  $k$  odd, the  $\sin(\pi kr/R)$  term can be rewritten as  $\sin(2\pi j_0 r/R + \pi \Delta k r/R)$  where  $\Delta k$  is an odd integer, and expanded using the basic trigonometric identity:

$$\sin\left(\frac{\pi kr}{R}\right) = \sin\left(\frac{2\pi j_0 r}{R}\right) \cos\left(\frac{\pi \Delta k r}{R}\right) + \cos\left(\frac{2\pi j_0 r}{R}\right) \sin\left(\frac{\pi \Delta k r}{R}\right) \quad (13)$$

Since  $\Delta k$  is odd, the first term in (13) averages to zero, but the second term will give nonzero projections on all the model cosine functions, decreasing as  $1/\Delta k$ .

If  $n = 2$ , then there are contributions from  $a_{ij}$  for  $j = 0$  (the spatial mean term), and  $j = k$ , because the  $\sin^2(\pi kr/R)$  term is equivalent to  $[1 - \cos(2\pi kr/R)]/2$ . This can be continued to all orders of  $n$ , giving sensitivity to increasingly high harmonics of range (and to the spatial mean). The limits of this high wave number information depend on the richness of the harmonics of  $G_{ik}(r)$ . If extra instruments are added off the axis, then the cosine terms in the model are better represented in the data. The extra multipaths also contribute to the degrees of freedom for reducing the effects of noise which in turn improves the sensitivity of the higher harmonics.

This analysis shows that there is a drop in the response of the travel time data to the spectrum of possible ocean perturbations between the mean term ( $j = 0$ ) and the harmonic corresponding to the ray with the fewest turning points ( $j = k_{\min}/2$ ). On the other hand, the various sources of distortion from sinusoidal ray weighting contribute to sensitivity at wave numbers (far) above  $j = k_{\max}/2$ . The more irregular the vertical structure function, the more high wave number resolution is available. By this reasoning, mode 2 should have more high wave number resolution than mode 1, given similar energies. Rays which are reflected from the surface have a richer set of harmonics, and so contribute more strongly to sensitivity to small scales. These predictions can be checked numerically, and some simulations are described below, using actual ray paths and mode functions. The analysis includes inverse calculations for these data sets to check how well the sensitivity can predict the performance of the reconstructions. The calculations which show sensitivity to components with  $j > k_{\min}/2$  (and of lack of sensitivity to  $0 < j < k_{\min}/2$ ) do not depend on the details of the inverse methods.

#### NUMERICAL RESULTS: SENSITIVITY

The numerical simulations in this section are related to work described by Howe *et al.* [1987], the analysis of data from a reciprocal tomographic experiment in the POLYMODE region. The sound speed profile in Figure 1 was made from hydrographic data taken during that experiment. A previous simulation study [Howe, 1987] used a truncated model (minimum wavelength of 300 km) to produce error maps for physical space using least squares

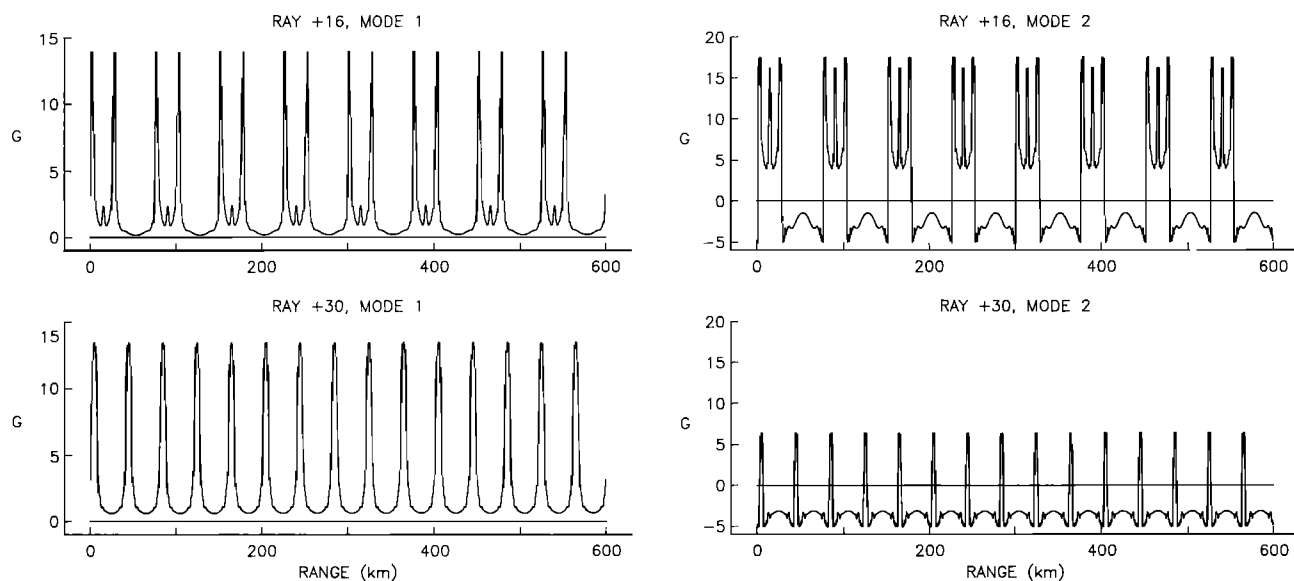


Fig. 5. Examples of the ray weighting functions (equation (7)) for two rays: a near-axial ray (+30) and a ray with large excursion (+16). The weighting functions are shown for both modes 1 and 2. The units are arbitrary.

inverses with varying numbers of receivers. In the simulations described here the source and receiver were both sited at 1350 m depth, near the sound speed minimum. The range ( $R$ ) between source and receiver is 600 km, which is also the domain of the spectral functions. Wave number 1 thus has one cycle in 600 km, wave number 10 has 10 cycles (60-km wavelength), and so on. The model parameterization is exactly periodic in  $R$ , but this could be eliminated by the addition of a trend term, as in time series analysis, without changing the results. (Malanotte-Rizzoli [1985] found some sensitivity to a ramp function in long-range tomographic data.)

Figure 5 shows examples of the ray weighting functions (equation (7)) for two of the rays shown in Figure 2. The first has identifier +16, meaning that it begins traveling upward from the source and has 16 turning points (eight double loops) between source and receiver. This ray has the longest double-loop range in the 24-ray data set (67 km), and has the largest excursion from the sound channel. The weighting function is exactly periodic in the 600-km domain, which is a consequence of the equal depths of source and receiver. The triple peaks result from the double humps in both modes, although the two modes can be easily distinguished. The second ray has identifier +30, and so has a double-loop range of 40 km. This ray remains much nearer to the sound channel axis, and so does not see the double peaks of either mode. The area under a single peak is marginally smaller than for the triple peaks of the first ray, consistent with the dependence on ray excursion derived in (11) and (12), but the larger number of peaks compensates. The nonnegativity of the weighting function for mode 1 contrasts with the function for mode 2, which is important for unscrambling the two modes in the inverse. The nonnegativity also ensures that the spatial mean of the anomaly field projects strongly on the ray travel times. In fact, for both modes, the area under the complete ray weighting curves is significantly nonzero, so the spatial mean (or range average) is strongly represented in the acoustic data. If the ray

paths and the mode shapes are exactly antisymmetric around the sound channel axis, then the spatial mean does not affect the data.

The spiky weighting functions have a rich harmonic content, and the periodicity (with fundamental wave number equal to half the number of turning points) means that the transform is also approximately a spaced set of spikes [Bracewell, 1978]. Figures 6, 7, and 8 show the spectrum of projections of the ray weighting functions on the model functions (the transform of the weighting function), as in (11) and (12), for three selected rays out of this data set. These spectra we call sensitivity spectra. Each figure displays the magnitudes of the projection (average of squares of sine and cosine components) for the first and second modes and the separate cosine and sine projections for modes 1 and 2, as a function of wave number,  $0 \leq j \leq 64$ . The mode amplitudes have been assigned according to the prior expectations for their magnitudes, so the first mode has 5 times the amplitude of the second. The travel time contribution per model parameter has been divided by an assumed noise level of 1 ms to nondimensionalize and provide a measure of significance. The horizontal line on the figure indicates unit signal to noise ratio. The ray with  $k = 16$  has the expected sharp peak at  $j = 8$ , replicated at 16, 24, and so on up to the maximum wave number in the model,  $j = 64$ . The amplitude of the sine component is about 4 times larger than the cosine term in the first peak, (which is difficult to see in the log scaling), and the cosine dominates at  $j = 16$ , as predicted for symmetric rays. There is no consistent dominance in the higher harmonic terms. This ray has the lowest fundamental periodicity in the data set, and so little information is expected for  $0 < j < 8$  in the inverse estimates from the data set. This ray also has approximately the largest excursion of any in the data set from Figure 2, and so was predicted to have the most energetic harmonics, although this ignored the effect of the number of loops.

Figure 7 shows that the projections for the most nearly

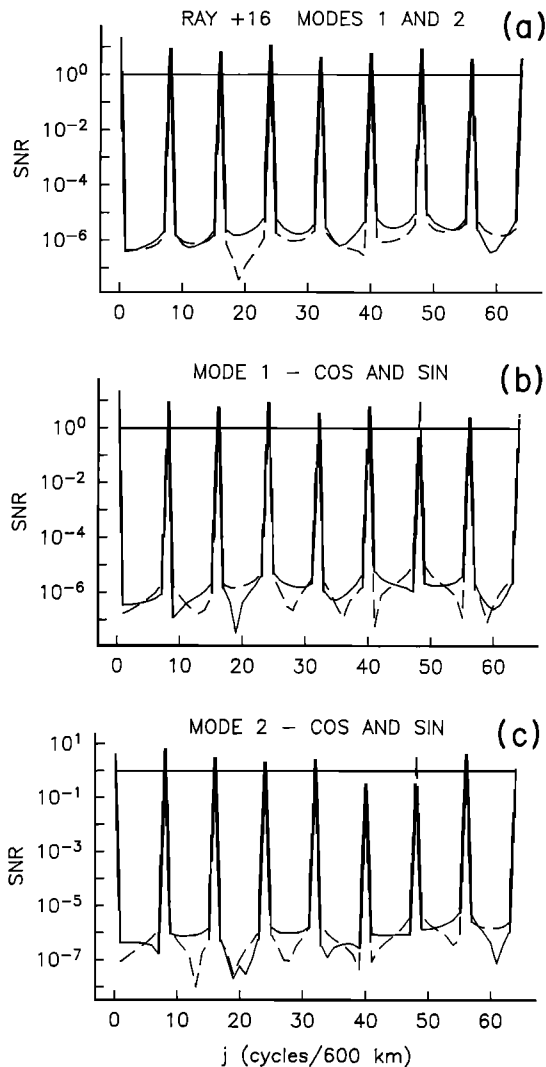


Fig. 6. Rms sensitivity spectrum for the +16 turning point ray, as a function of model wave number and vertical mode (equations (11) and (12)). (a) Sum of sine and cosine transform magnitudes as a function of wave number,  $0 \leq j \leq 64$ , for the first (solid line) and second (dashed line) modes, (b) Cosine (solid line) and sine (dashed line) transforms for mode 1. (c) Cosine (solid line) and sine (dashed line) transforms for mode 2. The horizontal line on the figure indicates unit signal to noise ratio, as described in the text.

axial ray ( $k = 30$ ) have a reduction in peak height with increasing harmonic which is slightly faster than in Figure 6, but the difference is not pronounced. The amplitude of the ray excursions around the axis also seem to have little effect, probably due to the concentration of the mode functions near the axis.

The ray with  $k = 17$  is confined almost entirely to cosine terms and has a much broader spectrum of projections, falling off approximately as  $1/\Delta k$  below and above the ray wave number, consistent with (13). The projection on  $\cos(2\pi 8r/R)$  ( $\Delta k = 1$ ) and the lower wave numbers ( $\Delta k = 3, 5, \dots$ ) are about twice the projections on  $\cos(2\pi 9r/R)$  ( $\Delta k = -1$ ), and the higher wave numbers ( $\Delta k = -3, -5, \dots$ ). This behavior is also repeated in the higher harmonics, and is not presently understood. The projection only on cosine terms occurs because the periodicity of the basis is exactly equal to the periodicity of the

rays. If, for example, the model functions were periodic on  $2R$  (1200 km), then this ray would project exactly on the  $j = 17$  component of that set. Since the ocean is not periodic on any scale, we should choose a domain larger than  $R$ , but the model parameters are not independent (orthogonal over  $R$ ) unless the model and data domains match. The lack of independence does not affect the inverse or the output estimates of ocean structure, but does complicate the intermediate displays, so we have retained this particular idealization in the simulations.

Figures 6, 7, and 8 suggest that there is useful information far beyond the parameterization cut off of  $j = 64$  (9.2-km wavelength), which is consistent with the sharpness of the peaks in Figure 5. The model was limited to a maximum wave number of 64 partly for simplicity and partly because only a limited number of rays were to be used in the inversions, so the accuracy of the estimates made from the data set was expected to taper off before reaching the cut off wave number. The number of rays in these simulations is arbitrary. If the number of sources and receivers on each mooring are both doubled, the

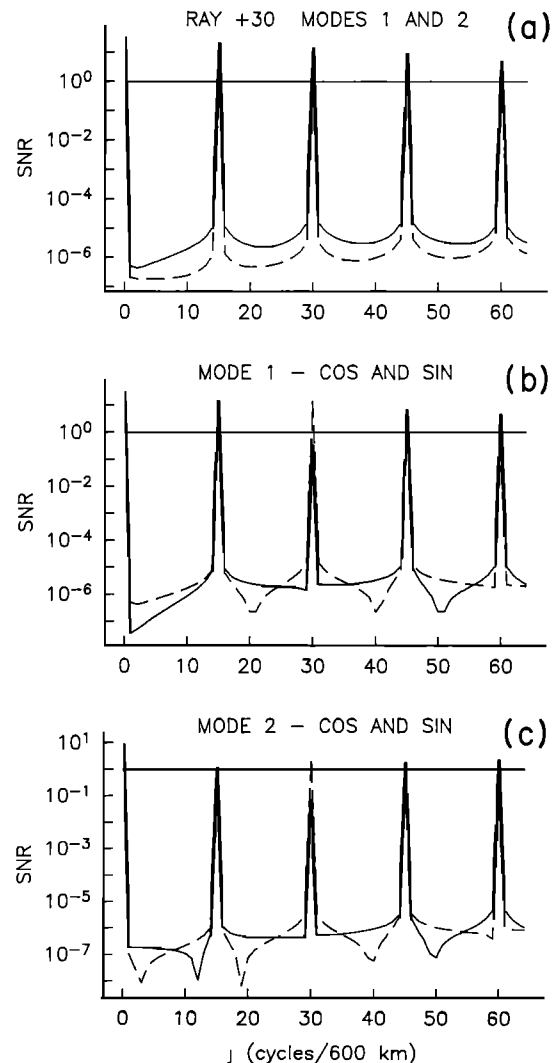


Fig. 7. Rms sensitivity spectrum for the +30 turning point ray, as a function of model wave number and vertical mode. See description of Figure 6.

amount of data is quadrupled [Munk and Wunsch, 1979], so it is possible to greatly increase the size of the data set. Additional instruments would also improve sensitivity to the cosine terms and fill in the gaps which are emphasized by the symmetries of the limited data set.

We have concentrated on spectral analysis, but the analysis in physical space, covered by Howe [1987], is a necessary part of the design of a tomographic system. A feature is invisible to rays which do not penetrate. Thus, for example, a surface-intensified mode affects only the rays with large vertical excursions, so that the inclusion of surface-reflected rays would improve the observability of the surface layer [Gaillard and Cornuelle, 1987].

The sharpness of the ray weighting functions determines the upper bound on the spatial resolution available for a given mode. If enough rays are available, then the position of a small ocean perturbation (which affects only a subset of rays) can be determined accurately with an uncertainty equal to the width of the weighting function peak. If the perturbations are too large (larger than any ray double-loop range), then there is an uncertainty in its location because all the rays in the data set will be

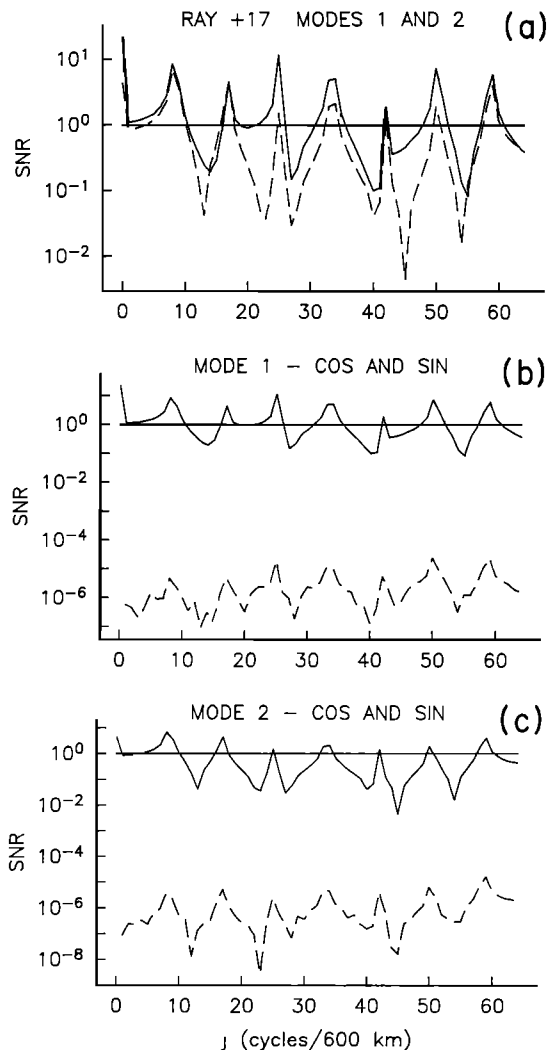


Fig. 8. Rms sensitivity spectrum for the +17 turning point ray, as a function of model wave number and vertical mode. See description of Figure 6.

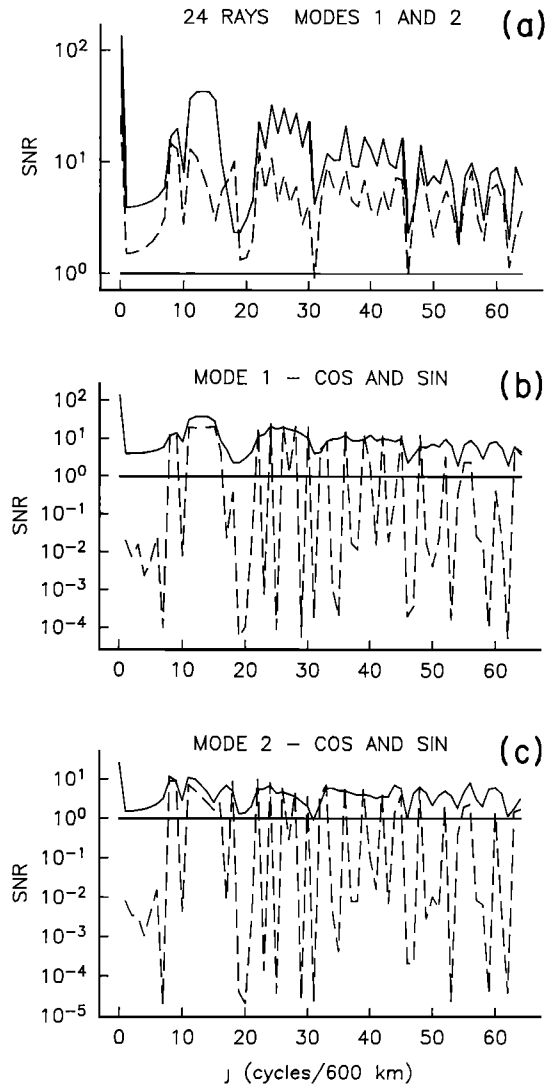


Fig. 9. Rms sensitivity spectrum for the 24-ray data set corresponding to Figures 2 and 3. The plots are similar to Figures 6, 7, and 8, but refer to all 24 rays instead of a single ray.

affected. Furthermore, it is necessary to have unique ray weighting functions for the different modes in order to be able to distinguish them. As an example, Figure 5 shows the weighting functions for the first two modes. There are significant differences between them so that the inverse should be able to unscramble the mode contributions. Note that a set of layers would be simpler to distinguish, since the contributions from different layers for a single ray would not overlap at all in range.

Superposing the magnitudes of the sensitivities of all the rays in the data set yields a combined sensitivity spectrum for the data set, which shows the rms travel time dependence for each model parameter. This partially predicts the quality of the inverse maps made from the data set, since model components that are well observed are more likely to be accurately estimated than those that are poorly observed. Figure 9 shows the rms sensitivity for the 24-ray data set corresponding to Figures 2 and 3. The sine component has many more deep valleys than the cosine components, because the odd-numbered rays project only on the adjacent cosine terms (equation (13)).

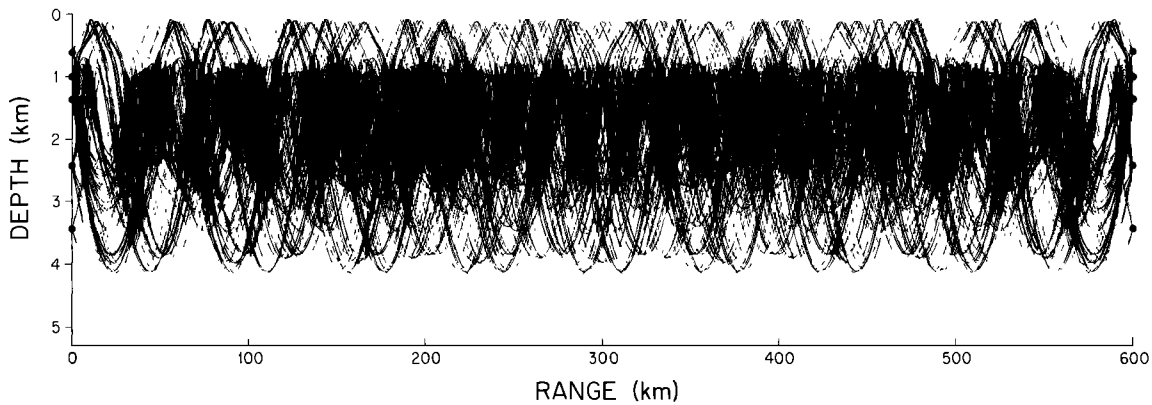


Fig. 10. Eigenray paths for the 156-ray data set obtained by adding four receivers to each mooring. The sources are at 1350 m depth on each mooring, and the receivers are at 600, 1000, 1350, 2400, and 3400 m. The 156 rays plotted are a subset of all those available for this geometry and sound speed.

The mean component is the strongest, and the gap between the mean and the lowest ray path harmonic is very pronounced. The valleys at wave number 10, 20, and 30 reflect the lack of rays with 20 (or 40) turning points in the data set. These rays (with identifier  $\pm 20$ ) have upper turning points in the low sound speed gradient at 300–700 m depth caused by 18°C water, and so are strongly affected even by small perturbations at these depths. For this reason, they were omitted from the data set of *Howe et al.* [1987] and *Howe* [1987], and from here. In these earlier studies the significance of these rays was not clear, and no special effort was made to include them.

The decrease of sensitivity with increasing wave number is best seen in Figure 9a. There is considerable ripple superimposed on the trend, but the falloff is relatively gentle. The falloff can be reduced and the overall significance of the observations can be improved by adding instruments to the moorings, thereby increasing the number of ray paths. Following *Howe* [1987], four receivers were added to each mooring (because receivers are relatively inexpensive to deploy compared to sources), giving a total data set of 156 rays (Figure 10). The reduced symmetry resulting from the additional instruments smooths the spectrum of the sine terms, and both spectra are filled in and raised in significance (Figure 11). The spectral gap at wave number 20 has become particularly obvious, since the adjacent components,  $j = 19$  and 21, are poorly observed due to the lack of rays with fewer than 16 turning points. There is significant sensitivity at the upper limits of the model, giving rise to a promise of accurate reconstructions at still smaller scales.

#### NUMERICAL RESULTS: INVERSE

The objective mapping procedure that was used in previous tomography experiments [*Cornuelle et al.*, 1985; *Howe et al.*, 1987] produced physical space error maps, commonly used in tomography array design. These error maps did not reveal the drops in sensitivity at certain wave numbers that are clearly shown in the above analysis. Thus array spectral analysis complements physical space methods. The spectral analysis shown so far merely indicates the presence or absence of observations of a particular model component. A rigorous inverse with error calculations is necessary to verify the mapping power of these

data sets, although the performance of the inverse can be predicted to some extent by the cumulative signal-to-noise for a given model parameter.

Estimates and expected errors were calculated for the

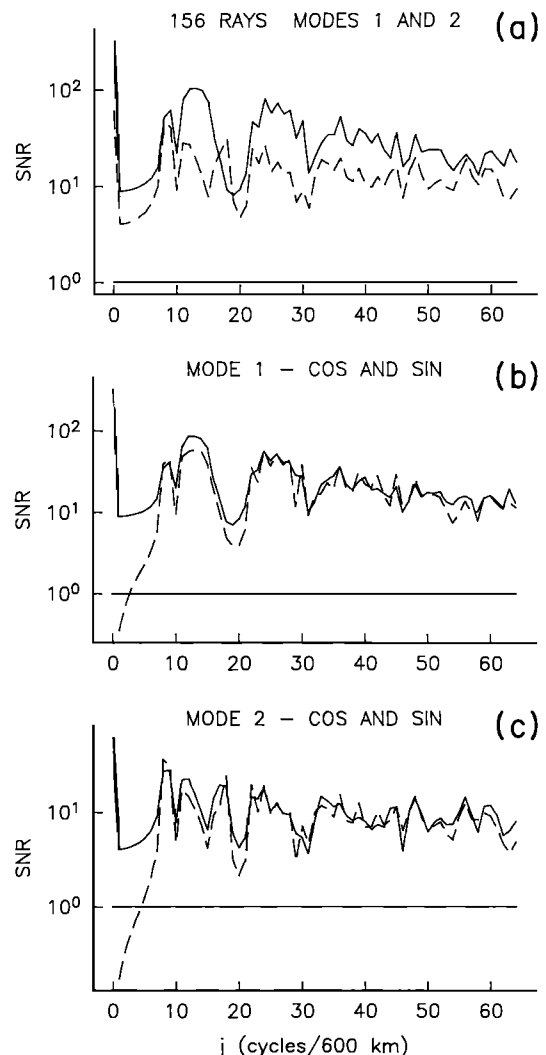


Fig. 11. Rms sensitivity spectrum for the 156-ray data set corresponding to Figure 10. Same as Figure 9, but for the 156-ray data set.



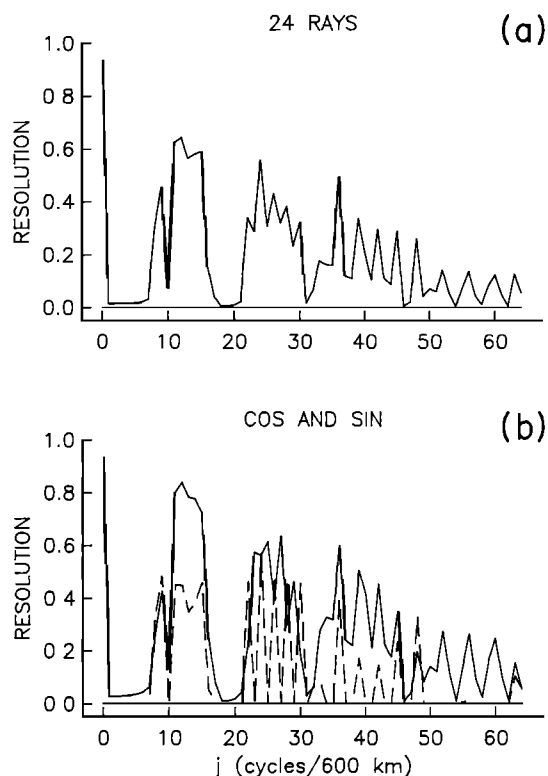


Fig. 12. "Transfer function" (the diagonal elements of the resolution matrix) for the 24-ray, single mode inverse with a data error of 1 ms and a white spectrum for the horizontal structure. (a) The total resolution. (b) The cosine (solid line) and sine (dashed line) components.

model parameters (with only one mode) using the 24- and 156-ray data sets described above. The rms travel time measurement error was taken to be 1 ms for all rays, and the expected energy of the field was set to a realistic value. Several inverses were performed using a weighted, tapered, singular value decomposition, which approximates the Gauss-Markov linear inverse operator. The spectrum of wave numbers was first assumed to be white, to remove the effect of expected energy on the accuracy of the estimate. (If an inverse is constructed with a spectrum which assumes no energy in the small-scale features, then they are ignored in the output estimates.)

The expected accuracy of the inverse reconstruction is described by the resolution matrix, which is square and maps the input (true) values of the model parameter to the output (estimated) values calculated by the inverse [Aki and Richards, 1980]. Column  $m$  of the resolution matrix quantifies the spreading by the inverse operator of a unit amount of parameter number  $m$ . If the column is zero except for unity at position  $m$ , then parameter number  $m$  is perfectly resolved by the inverse. A value of 1 on the diagonal indicates perfect resolution, while a value of zero means that all the variation corresponding to that model component is ignored by the data and/or misinterpreted by the inverse operator. The diagonal of the resolution matrix is thus a pseudo transfer function, and the value can be thought of as the gain through the observation-inverse system for each model parameter.

Figure 12 shows the "transfer function" for the 24-ray data set, assuming that only the first mode is important.

The mapping accuracy resembles the observation spectra at low wave number, but the higher wave numbers are necessarily poorly mapped because 24 data can only estimate a maximum of 24 independent quantities. Figure 13 gives the transfer function for the 156-ray data set. The similarity to the sensitivity spectra is close throughout the domain, including the spectral gaps.

When the second mode is included, the resolving power is divided between the modes, and the high wave number cutoff for mode 1 is reduced, although not by half, because the second mode is less energetic. This can be counteracted by adding more rays, since the sensitivities to the two modes are roughly comparable in size, but distinguishable (see Figures 9 and 11). The model can be extended to additional modes, within limits set by computer memory and computational expense. In practical array design, the expected energy levels of the modes and the expected spectra of their coefficients would determine the number of instruments and signal-to-noise levels needed. For the purposes of this simulation, only the mode 1 cases were treated in detail, in order to limit complication and costs. The sensitivity spectra, and thus the conclusions we have drawn from them, are independent of mode shape (including layer models), provided the weighting functions are sharp and distinguishable.

Figures 14 and 15 present two examples in which small-scale test patterns are reconstructed using 24- and 156-ray travel time data, respectively, and white prior spectra. Both a step function centered between the moorings and a 10-km Gaussian "eddy" in the same place show essentially the same results. The midpoint of the range between moorings is the point where the error maps of Howe [1987] showed the poorest performance; near the

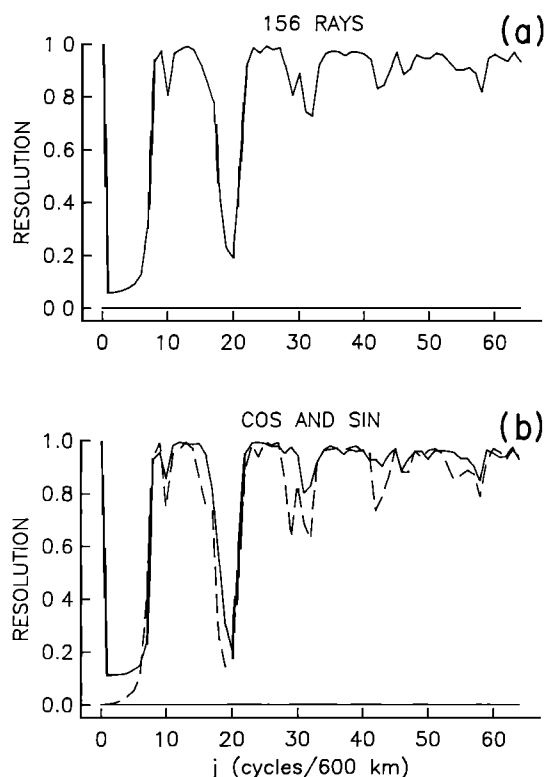


Fig. 13. Same as Figure 12, but for the 156-ray data set.

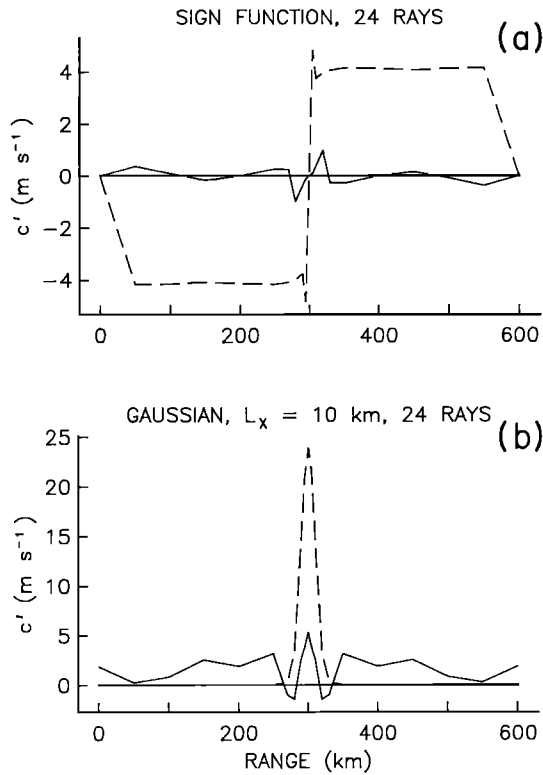


Fig. 14. True ocean (dashed line) and inverse reconstruction (solid line) for the inverse which used 24 rays and a white prior spectrum for the horizontal variation of the amplitude of mode 1 (the inverse transfer function is plotted in Figure 12).

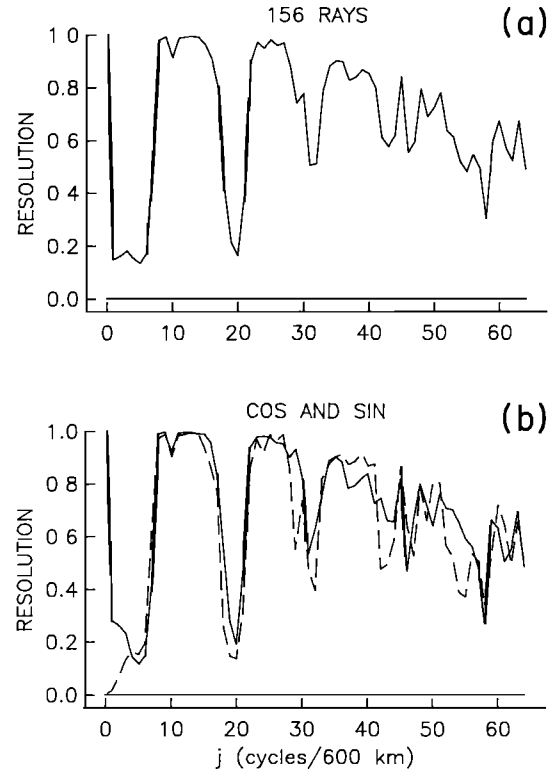


Fig. 16. Same as Figure 12, but for the 156-ray data set with an expected variance spectrum (for mode 1) that is constant for wave numbers  $j = 1$  to 3 and decreases as  $j^{-2}$  for  $j > 3$  (wavelengths smaller than 200 km).

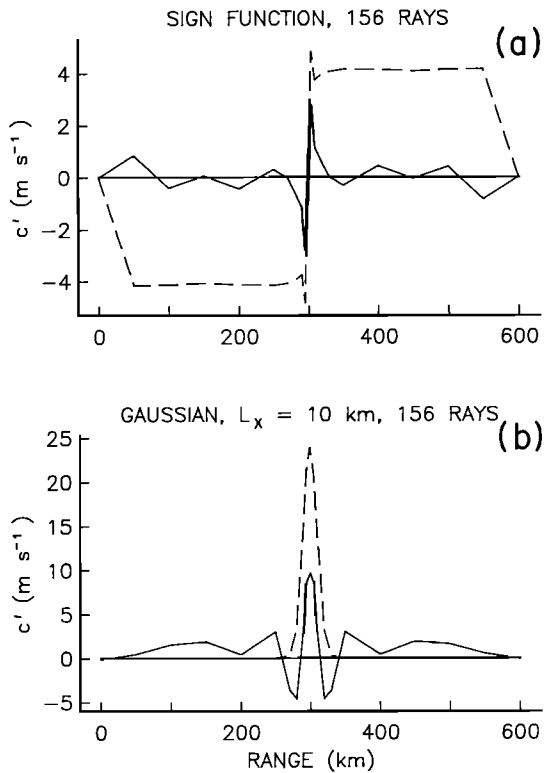


Fig. 15. Same as Figure 14, except for the inverse which used 156 rays. (The inverse transfer function is plotted in Figure 13.)

moorings the accuracy improves. The 24-ray reconstruction performs relatively poorly, as expected, and yet still gives some indication of the feature location. In both inverses, the test pattern is "high-pass filtered," as in the resolution analysis, and the spatial mean is well resolved. The shapes and locations of the small features are preserved, but larger scales are filtered out.

As a final, perhaps more realistic, example, we assume a prior variance spectrum that is white up to wave number  $j = 3$  and then decreases as the inverse square of wave number. This spectrum has an rms bandwidth of approximately 10 cycles per 600 km corresponding to a 60-km correlation length scale. The transfer function that results using this spectrum with only mode 1 is shown in Figure 16. The estimation of the low wave number components improves (as compared with the white spectrum case (Figure 13), but the mapping accuracy declines at high wave numbers (above  $j = 40$ , or 15-km wavelength). Given the 1-ms errors, the small scales have poor signal-to-noise ratios with this spectral weighting, and decreasing the measurement errors would improve the high wave number performance.

To simulate one realization of a sound speed field with this spectrum, random phases were used for each spectral component. The realization and corresponding inverse estimate are plotted in Figure 17a. The two agree near the ends but disagree in the interior, most notably between 250 and 500 km where two large, low-wave number features are present. The high-pass versions ( $j \geq 8$ ) of the true and estimated sound speed agree very well (Fig-

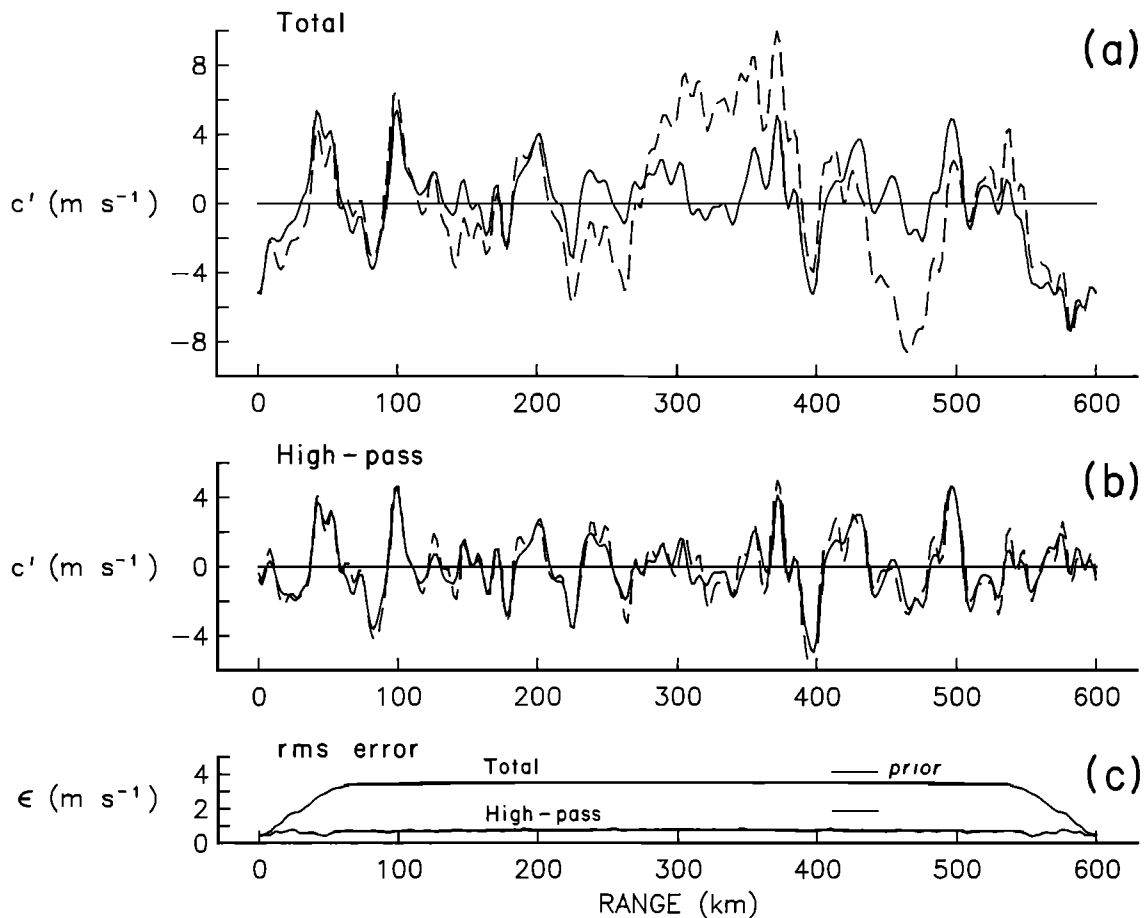


Fig. 17. One realization of sound speed perturbation for the case described in Figure 16. (a) The total sound speed perturbation at 1000 m, true (dashed line) and estimate (solid line). (b) The high-pass sound speed perturbation. (c) Estimated rms errors for the total high-pass estimates. The lines labeled prior show the uncertainty in the absence of any data (i.e., variation relative to  $c_0$ ). The inverse transfer function is plotted in Figure 16.

ure 17b); the correlation coefficient is 0.94. The estimated errors are consistent with these results (Figure 17c). The total error is a minimum at each end and increases over the 60-km correlation length scale to a relatively large constant value in the interior. We associate this reduction of error near each end with the asymmetric fanlike structure of the ray paths. The high-pass errors are significantly reduced from the a priori values because of the good resolution in this range of wave numbers.

These examples show that large errors in the total sound speed are possible at any point, consistent with the error bars of Howe [1987]. On the other hand the errors are limited to relatively large scales. Large-scale errors might be ignored for feature identification and monitoring or for high wave number spectra. The missing information could be supplied by alternate observation methods or (possibly) by dynamical inverse methods.

#### DISCUSSION

Both the analytical theory and the numerical simulations presented above show that the data used in single-slice acoustic tomography are more sensitive to features with scales shorter than the maximum ray double-loop length (about 100 km) than to features with larger scales, up to the range of the transmissions. The spatial mean between

moorings is reconstructed well, as are the components of the field with wavelengths shorter than the double-loop length. The high wave number information has not been exploited by single-slice tomography experiments to date, which have concentrated on reconstruction of spatial mean currents and sound speed perturbations [Howe *et al.*, 1987]. The sensitivity to small scales was not suspected in previous studies because rms sensitivity to the wave numbers just above the spatial mean is down by more than 1 order of magnitude for both examples, and the reconstructions are poorer by at least the same factor. The sensitivity radically improves for the components with wavelengths of 60 km or less, and the reconstructions can be nearly perfect at these scales. The gap is a consequence of the ray geometries imposed by the realistic ocean waveguide assumed in the calculations, and would not be present if rays with double-loop ranges longer than 100 km were available. The sound speed profiles used in the simulations are typical for the North Atlantic subtropical gyre. Ray paths for North and equatorial Pacific sound channels show similar maximum double-loop ranges. The finite depth of the ocean is responsible in part for the constraints on the rays, since an infinitely deep ocean (with increasing sound speed with depth) would allow surface-reflected rays with long double-loop ranges.

Previous studies of acoustic tomography have relied

largely on numerical simulations which truncated the ocean parameterization at a relatively low wave number. Simulation results [Howe, 1987] showed disappointing reconstructions of range-dependent sound speeds for source-receiver ranges greater than about 300 km, using a parameterization which allowed no wavelengths as short as ray double-loop ranges. The results were displayed as maps of expected error variance in the reconstructions as a function of range and depth. The errors were small near the sources and receivers, but increased toward the interior of the section; at a distance of more than 100 km from the instruments the error variance approached the prior variance of the horizontally varying components of the parameterization. Increasing the number of instruments produced only slight improvement in the reconstructions for 600-km transmissions, although decreasing measurement errors by an order of magnitude (to about 0.1 ms) did improve the reconstructions.

The spectral analysis can provide some explanation and qualification of these results. The regions near the instruments are distinguished from the interior of the profile because the ends of the section break the symmetry of the ray paths. Perturbations can thus be localized uniquely within about one half of a ray double-loop length of each instrument. In the interior, the relatively low sensitivity to medium scales takes over. The analytical theory does not exclude the possibility of good reconstructions at low wave number, but the sensitivity to 100- to 600-km scales depends on asymmetries, and is down roughly by 1 order of magnitude compared to the high wave number effects. Depending on spectral shape, this difference in sensitivity may be balanced by the greater energy in the larger scales, to make the transfer function of the tomographic observations more uniform.

Increasing the number of rays mainly improves the reconstructions of the small scales (Figures 9–13), but the rms sensitivity to the wave number band above the mean is increased, although still relatively small. Reducing the assumed measurement errors by a factor of 10 makes the sensitivity to the medium scales significant. This suggests that increasing the number of instruments on each mooring beyond one source and five receivers could enable useful reconstructions of wavelengths longer than the ray double-loop length. In particular, increasing the number of sources increases the variety of rays in the data set, and should improve the reconstructions. Because the sensitivity to intermediate scales depends on asymmetries in the ray paths, high measurement precision is critical for good mapping.

In previous tomographic inverses, scales smaller than 100 km were omitted from the parameterization and so the travel time perturbations from scales smaller than the cutoff must be added to the measurement noise. The division between "signal" and "noise" is controlled by the truncation of the parameterization; as the model is extended to smaller scales, the effective noise level in the data drops until it is controlled by other errors. The ultimate limits on arrival time measurement precision are somewhere below 0.1 ms for the cases we are considering, but the dominant error term is likely to be due to deviations of the ray paths from the assumed path. This nonlinearity has been studied in several contexts [Spiesberger

and Worcester, 1983; Mercer and Booker, 1983; Spiesberger, 1985; Munk and Wunsch, 1985, 1987]. The path nonlinearities can be of the order of 3 ms for a 600-km range, so they would dominate the error budget if uncorrected. One way to correct for path changes is to iterate the inverse using the estimates of the sound speed and current fields to retrace the rays in the data set to make the paths more nearly correct. This requires good mapping of all scales if the iteration is to converge correctly.

If ray path nonlinearity can be avoided, then the measurement noise decreases as the model is extended and useful estimates might be made at very small scales. As the precision increases, the sensitivity to large scales becomes significant, and extending the model to small scales could improve the reconstruction of the large scales.

There are other means of removing the spectral gap between the mean and the longest ray double-loop wavelength. With a number of moorings in a horizontal array, as in the 1981 experiment [Ocean Tomography Group, 1982], the crossing ray paths in the horizontal supply the low-wave number information. In a single vertical section, expendable bathythermograph or air-dropped expendable bathythermograph drops at about 100-km spacing could fill the gaps. Even a limited set of multipaths, as in the examples, contains information at the spatial frequencies important for vorticity dynamics. The complete inverse problem should include dynamical constraints to infer the large-scale structure given good estimates of the evolving small scales. For example, in a strongly nonlinear feature, such as a modon, the relations between scales might be used to reconstruct the entire feature given only high-pass information. Extending the model to scales of order 1 km would involve a much broader spectrum of vertical motion, and would complicate the dynamics needed for time-dependent reconstruction.

Tomographic multipath data in a long vertical slice can act as an edge enhancer for detecting and/or monitoring sharp features. Images are often high-pass filtered to emphasize boundaries between uniform regions, and tomography could provide such "enhanced" images of the ocean. Data from a pair of dense vertical arrays separated by 300 to 1000 km can produce spectra for wavelengths shorter than 100 km, perhaps including the region of transition between planetary waves and internal waves. The high-wave number limits of sensitivity as the number of instruments becomes large were not tested by the examples, but the sharpness of the peaks in the ray weighting functions suggests the possibility of accurate reconstructions of scales of the order of a few kilometers, even over large regions, given sufficient high-precision rays.

*Acknowledgments.* Thanks to W. Munk and P. Worcester for careful readings and suggestions. Elaine Blackmore prepared the final manuscript and Don Betts prepared the figures. This work was supported by ONR contracts N00014-85-C-104 and N00014-80-C-0217 and NSF grant OCE-8414978.

## REFERENCES

- Aki, K., and P. G. Richards, *Quantitative Seismology: Theory and Methods*, W. H. Freeman, San Francisco, Calif., 1980.
- Bracewell, R., *The Fourier Transform and Its Applications*, McGraw-Hill, New York, 1978.
- Brown, M. C., Application of the WKBJ Green's function to

- acoustic propagation in horizontally stratified oceans, *J. Acoust. Soc. Am.*, 71, 1427–1432, 1982.
- Cornuelle, B., C. Wunsch, D. Behringer, T. Birdsall, M. Brown, R. Heinmiller, R. Knox, K. Metzger, W. Munk, J. Spiesberger, R. Spindel, D. Webb, and P. Worcester, Tomographic maps of the ocean mesoscale: Pure acoustics, *J. Phys. Oceanogr.*, 22, 133–152, 1985.
- Flatté, S. M., and R. B. Stoughton, Theory of acoustic measurement of internal wave strength as a function of depth, horizontal position, and time, *J. Geophys. Res.*, 91, 7709–7720, 1986.
- Gaillard, F., and B. Cornuelle, Improvement of tomographic maps by using surface-reflected rays, *J. Phys. Oceanogr.*, in press, 1987.
- Howe, B. M., Multiple receivers in single vertical slice ocean acoustic tomography experiments, *J. Geophys. Res.*, 92, 9479–9486, 1987.
- Howe, B. M., P. F. Worcester, and R. C. Spindel, Ocean acoustic tomography: Mesoscale velocity, *J. Geophys. Res.*, 92, 3785–3805, 1987.
- Malanotte-Rizzoli, P., Long-range inversions for ocean acoustic tomography, *J. Geophys. Res.*, 90, 7098–7116, 1985.
- Mercer, J. A., and J. R. Booker, Long-range propagation of sound through oceanic mesoscale structures, *J. Geophys. Res.*, 88, 689–699, 1983.
- Munk, W. H., and C. Wunsch, Ocean acoustic tomography: A scheme for large scale monitoring, *Deep Sea Res.*, 26, 123–161, 1979.
- Munk, W., and C. Wunsch, Biases and caustics in long-range acoustic tomography, *Deep Sea Res.*, 32, 1317–1346, 1985.
- Munk, W., and C. Wunsch, Bias in acoustic travel time through an ocean with adiabatic range-dependence, *Geophys. and Astrophys. Fluid Dyn.*, in press, 1987.
- Ocean Tomography Group, A demonstration of ocean acoustic tomography, *Nature*, 299, 121–125, 1982.
- Spiesberger, J. L., Ocean acoustic tomography: Travel time biases, *J. Acoust. Soc. Am.*, 77, 83–100, 1985.
- Spiesberger, J. L., and P. Worcester, Perturbations in travel time and ray geometry due to mesoscale disturbances: A comparison of exact and approximate calculations, *J. Acoust. Soc. Am.*, 74, 219–225, 1983.

---

B. Cornuelle and B. M. Howe, Scripps Institution of Oceanography, A-030, University of California, San Diego, La Jolla, CA 92093.

(Received April 11, 1987;  
accepted June 3, 1987.)